ARTICLE

Multifunctional targeted nanoprobe with high NIR-II PAI/MRI performance for precise theranostics of orthotopic early-stage hepatocellular carcinoma

Linyun He,‡[a,b,c,d] Yachao Zhang,‡[b,c] Jiangbo Chen,‡[b,c] Gongyuan Liu,[e] Jingyi Zhu,[b,c] Xiaozhen Li,[e,f] Dengfeng Li,[b,c] Yuqi Yang,[g] Chun-Sing Lee,[e,f] Jiahai Shi,[g] Chao Yin,*[h] Puxiang Lai,*[i,j] Lidai Wang,*[b,c] and Chihua Fang,*[a,d]

Early diagnosis and effective treatment of hepatocellular carcinoma (HCC) is quite critical for improving patients' prognosis. The combination of second near-infrared window photoacoustic imaging (NIR-II PAI) and T2-magnetic resonance imaging (T2-MRI) is promising for achieving omnibearing information to HCC diagnosis due to complementary advantages of outstanding optical contrast, high temporospatial resolution and soft-tissue resolution. Thus, the rational design of multifunctional targeted nanoplatform with outstanding performance in dual-modal NIR-II PAI/T2-MRI is particularly valuable for precise diagnosis and image-guiding non-invasive photothermal therapy (PTT) of early-stage HCC. Herein, a versatile targeted organic-inorganic nanoprobe was synthesized as HCC-specific contrast agent for sensitive and efficient theranostics. The developed multifunctional targeted nanoprobe yielded superior HCC specificity, reliable stability and biocompatibility, high imaging contrast both in NIR-II PAI and T2-MRI, and excellent photothermal conversion efficiency (74.6%). Furthermore, the theranostic efficiency of targeted nanoprobe was systematically investigated *in vivo* using orthotopic early HCC-bearing mice model. The NIR-II PAI exhibited sensitive detection of ultra-small HCCs (diameter less than 1.8mm), and long-term real-time monitoring of tumors and nanoprobes targeting process in deep tissue. The T2-MRI demonstrated the clear imaging contrast and spatial relationship between micro-HCC and adjacent structures for comprehensive description of tumor. Moreover, upon using targeted nanoprobe, the non-invasively targeted PTT of orthotopic early HCC was carried out under the reliable dual-modal imaging guidance with remarkable anti-tumor efficiency and biosafety. This work provides insight into constructing multifunctional targeted nanoplatform for precise and comprehensive theranostics of early-stage HCC, which would greatly benefit the patients in the era of precision medicine.

[a.] Department of Hepatobiliary Surgery, Zhujiang Hospital, Southern Medical University, Guangzhou, 510280, China. E-mail: fangch_dr@163.com

[b.] Department of Biomedical Engineering, City University of Hong Kong, Hong Kong SAR, 999077, China. E-mail: lidawang@cityu.edu.hk

[c.] City University of Hong Kong Shenzhen Research Institute, Shenzhen, 518057, China

[d.] Guangdong Provincial Clinical and Engineering Technology Center of Digital Medicine, Guangzhou 510282, China

[e.] Department of Chemistry, City University of Hong Kong, Hong Kong SAR, 999077, China

[f.] Center of Super-Diamond and Advanced Films and Department of Chemistry, City University of Hong Kong, Hong Kong SAR, 999077, China

[g.] Department of Biomedical Sciences, College of Veterinary Medicine and Life Sciences, City University of Hong Kong, Hong Kong SAR, 999077, China

[h.] Key Laboratory for Organic Electronics and Information Displays, Jiangsu Key Laboratory for Biosensors & Institute of Advanced Materials, Jiangsu National Synergetic Innovation Center for Advanced Materials, Nanjing University of Posts & Telecommunications, Nanjing, 210023, China. E-mail: yinchao1990lover@163.com

[i.] Department of Biomedical Engineering, The Hong Kong Polytechnic University, Hong Kong SAR, 999077, China. E-mail: puxiang.lai@polyu.edu.hk

[j.] Hong Kong Polytechnic University Shenzhen Research Institute, Shenzhen, 518057, China

† Electronic Supplementary Information (ESI) available: The synthesis, characterization and the PCE calculation of targeted nanoprobe, the histological examination of HCC, LC and major organs, and the introduction of PA instruments. See DOI: 10.1039/x0xx00000x

‡ These authors contributed equally to this work.

Introduction

Hepatocellular carcinoma (HCC), predominantly occurs in the context of liver cirrhosis (LC) and other high risk factors, is one of the leading cause of cancer worldwide.[1,2] The overall 5-year survival (18%) and health benefit of treating HCC are limited because majority of patients are diagnosed at advanced stages.[3] Thus, it is urgent to improve the current diagnostic and therapeutic strategies, targeting patients at risk for sensitive detection and curative treatment of millimeter-sized early-stage tumor in the age of precision medicine.[4,5] Medical imaging plays a critical role in early tumor diagnosis with accurate differentiation between benign and malignant hepatic nodules. Among commonly used imaging methods for HCC detection,[4,6] magnetic resonance imaging (MRI) is widely used in clinic and competent to provide non-invasive anatomical and physiological information for early cancer diagnosis due to its high spatial and soft tissue resolution.[7] In particular, T2-weighted MRI offers potential to identify HCC in chronic liver disease, overcoming the renal toxicity caused by gadolinium-contrast in T1-weighted MRI.[8] However, the application of MRI

in identifying micro-HCC (diameter less than 10 mm) is hindered by limited sensitivity and temporal resolution.[9] Hence, the combination of T_2-MRI and other imaging method has great potential to provide complementary and comprehensive information for precision theranostics. As an emerging hybrid imaging technique, photoacoustic imaging (PAI) can realize *in vivo* real-time imaging with high temporospatial resolution and inherent optical molecular sensitivity,[10,11] lending clear advantages in retrieving micrometer-level, functional, and metabolic information in biological tissue over traditional optical imaging especially at the second near-infrared (NIR-II, 1000-1700 nm) window.[12-14] Therefore, the multimodal imaging of T_2-MRI with NIR-II PAI is desirable to overcome the respective limitations and achieving synergistic superiorities, which can provide omnibearing information of the early-HCC for precise diagnostic evaluation and subsequent treatment.[15,16]

Furthermore, according to the current guidelines, the local ablation has been considered as the first-line treatment in early-HCC patients with Barcelona Clinic Liver Cancer (BCLC) stage 0/A.[17,18] But the conventional ablation methods, including radiofrequency and microwave, rely heavily on the operator's skills and easily damage collateral normal liver tissue, bile duct or vessels.[19] Photothermal therapy (PTT) is a novel therapeutic approach that employs the photothermal agents (PTAs) to convert optical energy into heat for cancer ablation effectively.[20,21] Compared with traditional ablation, the PTT in the NIR-II window demonstrates greater prospects for tumor ablation in deep tissues with high selectivity, non-invasiveness and satisfactory therapeutic efficacy.[21-23] With these advantages, NIR-II PTT is also easily integrated with other imaging technique to incorporate multifunctional platform to accomplish optimized therapeutic efficiency.[24] Thus, the multifunctional strategy of dual-modal NIR-II PAI/T_2-MRI and imaging-guided non-invasive PTT were used in this study for precise theranostics of early-stage HCC and eventually improve the prognosis.

To further promote the theranostic efficiency of HCC, a multifunctional targeted nanoprobe should be developed as auxiliary contrast agent for current multi-modal theranostic platform,[25] which combines dual-modal imaging agent, therapeutic agent, and targeted linker into one entity. Among numerous nanomaterials for T_2-weighted MRI, the Fe_3O_4 magnetic nanoparticles (MNPs) have become the most promising contrast agent for practical application currently in tumor diagnosis due to outstanding properties including low toxicity, easy functionalization, better superparamagnetic behavior and relaxivity.[26,27] Meanwhile, the MNPs-enhanced T_2-MRI also exhibits advantage of differentiating HCC from other focal hepatic nodules (eg. LC) in animal model.[28] Besides, as a completely organic and biologically inert material, the semiconducting polymers (SPs) with strong charge transfer features can serve as the signal producers for PA molecular imaging and the photothermal conversion,[29-31] allowing non-invasive NIR-II PAI and PTT of deep tumor. Besides, the structural units of SPs can chelate metal ions, which is able to functionalize with MNPs to generate organic-inorganic hybrid nanomaterial easily.[32] Thus, the MNPs and SPs were finely

integrated into one nano-entity with the surface modification of polyethylene glycol (PEG) to fabricate the inorganic-organic hybrid multifunctional nanoprobe MNP-SP@PEG with easy functionalization, high stability, and biocompatibility. Additionally, active targeting to oncogenic biomarkers have become the hot topics in cancer research and help to realize the precision medicine.[33] Glypican-3 (GPC3) is a cytomembrane-anchored oncofetal protein that is overexpressed in up to 80% of HCC patients but is absent in normal tissues and cirrhotic liver.[34] GPC-3 has become a clinically-relevant biomarker for the diagnosis of early HCC.[35,36] When an anti-GPC-3 monoclonal antibody conjugated with the MNP-SP@PEG, the nanoprobe will target HCC actively, improving the therapeutic efficiency and avoiding toxicity to normal tissue. Consequently, an active novel GPC-3-targeted hybrid multifunctional nanoprobe (MNP-SP@PEG-antibody) was designed and fabricated for dual-modal NIR-II PAI/MRI and imaging-guided non-invasive PTT, permitting great potential for precise theranostics of orthotopic early-stage HCC.

In addition, most previous studies about diagnosis and PTT on HCC have mainly focused on ectopic subcutaneous tumor models,[25,37-40] lacking sufficient theranostic evidence in orthotopic HCC. And the tumor microenvironment and behavior are different between ectopic subcutaneous tumor models and orthotopic HCC model.[41] Meanwhile, there is an absence of diagnostic strategy for orthotopic HCC using dual-modal NIR-II PAI and T_2-MRI.[42-44] Besides, the very few studies on PTT for orthotopic HCC also require direct irradiation to the liver through laparotomy or laparoscopy with certain trauma.[43,44] Thus, it is of great significance to establish the orthotopic early-stage HCC model, providing more reliable evidence for future early diagnosis and treatment of human HCC as well as improving prognosis of high-risk patients.

In this study, we presented a versatile targeted organic-inorganic hybrid nanoprobe for multifunctional theranostic nanoplatform, which achieved the precise diagnosis and treatment of early-stage HCC. This novel GPC-3 targeted nanoprobe was first synthesized as the HCC-specific contrast agent *via* nanoprecipitation method, exhibiting excellent dual-modal imaging results in NIR-II PAI/T_2-MRI, high photothermal conversion efficiency, good biocompatibility, and active targeting ability. Compared to the LC mouse model, the early orthotopic HCC-bearing mouse model showed that abundant targeted nanoprobe could actively concentrate in tumor tissues specifically after systemic administration. Then the *in vivo* performance of NIR-II PAI/T_2-MRI present accurate diagnosis of micro-HCC and presents significant contrast with surrounding tissues, offering reliable guidance for subsequent PTT successfully with satisfied anti-tumor effect in a non-invasive manner (Scheme 1). This is the first report describing dual-modal imaging-guided non-invasive NIR-II PTT for orthotopic micro-HCC *via* the application of versatile targeted organic-inorganic hybrid nanoprobe. Thus, our work provides an optimized theranostic strategy for early-stage HCC especially in high-risk patients based on multi-functional nanoplatform in the era of precision medicine.
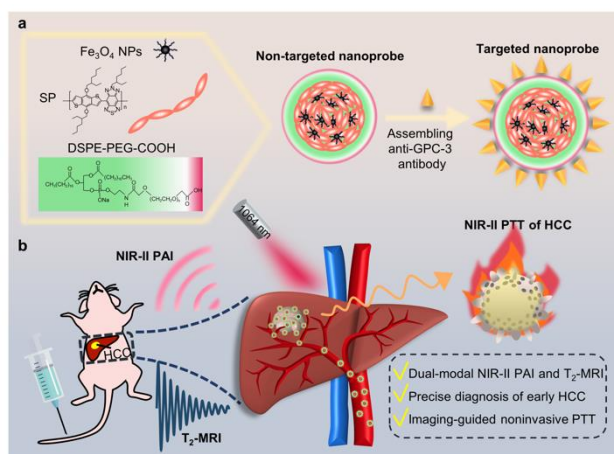
Scheme. 1 Schematic illustration of the precise diagnosis and therapy of orthotopic early-stage hepatocellular carcinoma. (a) Synthesis scheme of HCC-targeted nanoprobe. **(b)** Illustration of dual-modal NIR-II PAI/T_2-MRI and imaging-guided non-invasive PTT of early-stage orthotopic HCC after targeted nanoprobe injection.

Materials and methods

Synthesis of targeted nanoprobe.

The synthesis of MNPs, SP, and the fabrication process of HCC-targeted nanoprobe are presented in the Supplementary Information.

Cell culture.

HepG2 (human hepatocellular carcinoma cells, labelled with luciferase) and L-O2 cells (human normal liver cells) were cultured in a medium containing 89% Dulbecco's modified Eagle's medium (DMEM, Gibco), 10% fetal bovine serum (FBS), and 1% penicillin-streptomycin at 37 °C under a 5% CO_2 atmosphere.

Animal models.

BALB/c nude mice (female, 4-6 weeks) were purchased from the Laboratory Animal Service Center (LASEC, Chinese University of Hong Kong) to establish the orthotopic HCC model. The HepG2 cell suspension (1×10^6 cells in 50 µL PBS) was injected into the liver lobe *via* laparotomy. Approximately 10 days after tumor plantation, D-luciferin (150 mg kg^{-1}) was injected intraperitoneally into mice and combined with luciferase-labelled HepG2 cells. Then the engraftment of xenografts and tumor growth were evaluated by testing the bioluminescence of HepG2 cells using a small animal optical imaging system (In-Vivo Xtreme, Bruker, Germany). Early-stage HCC in nude mice is defined as a diameter less than 2 mm.[43]

In addition, healthy ICR mice (male, 6-8 weeks) were acquired from the Lab Animal Research unit (City University of Hong Kong) to induce the LC model. These mice were intraperitoneally injected with 20% carbon tetrachloride (CCl_4) solution diluted in olive oil (5 mL kg^{-1}) twice per week for 12 weeks.[45] All animal experiments were carried out in compliance with the guidelines of the City University of Hong Kong's animal ethical committee.

Photothermal properties of targeted and non-targeted nanoprobe *in vitro*.

The targeted and non-targeted nanoprobe aqueous dispersions of different concentrations (0, 25, 50, 100, and 200 µg mL^{-1}) were prepared to evaluate their photothermal properties. These dispersions were placed in quartz cuvette and continuously irradiated with a 1064 nm laser at a power density of 1 W cm^{-2} for 10 min. Temperature evolutions of all samples were recorded by an infrared thermal camera (FLIR One Pro, USA) and analyzed using the FLIR Tools software. In the photothermal stability test, the targeted and non-targeted nanoprobe dispersions were exposed to NIR-II light illumination for 10 min, followed by a natural cooling process to room temperature for three cycles. In addition, to measure the photothermal conversion efficiency (η) of targeted nanoprobe, the temperature changes of the solution (100 µg mL^{-1}) were recorded as a function of time during the natural cooling stage after reaching the maximal temperature plateau. Then η was calculated according to a previous report.[46,47]

Targeting ability of targeted nanoprobe *in vitro*.

The HepG2 and L-O2 cells were seeded in 60 mm-diameter Petri dishes at a density of 1×10^5 cells per dish and cultured for 24 h. Then the HepG2 cells were respectively incubated with targeted or nontargeted nanoprobe (50 µg mL^{-1}), while the L-O2 cells were treated with targeted nanoprobe (50 µg mL^{-1}) overnight. After washing with PBS three times, these cells were imaged by a lab-built optical-resolution photoacoustic microscopy (OR-PAM) [48] with a 532 nm pulsed laser to verify the binding ability of targeted nanoprobe, and the PA amplitudes were analyzed quantitatively to show the binding ability of nanoprobes to cells. The details of the OR-PAM system are provided in the Supplementary Information (Fig. S1, ESI†). The pulse energy was 75 nJ during imaging.

The Cell viability of nanoprobes.

The cytotoxicity of both targeted and non-targeted nanoprobe was evaluated using standard 3-(4,5-dimethylthiazol-2-yl)-2,5-diphenyltetrazolium bromide (MTT) assay method. HepG2 and L-O2 cells were seeded in 96-well plates at a density of 0.5×10^4 cells (200 µL) per well in the growth medium. After cells reached 70-80% confluence, fresh culture media containing different concentrations of targeted or non-targeted nanoprobe (0, 6.25, 12.5, 25, 50, and 100 µg mL^{-1}) were further used to co-incubate the above cells for 24 h in the dark. Then 100 µL MTT solution (0.5 mg mL^{-1}) was added to each well, followed by the addition of 150 µL dimethyl sulfoxide (DMSO) to dissolve the produced formazan crystals following the guidelines of the MTT assay. The cell viabilities were calculated based on the absorbance values at 570 nm using a microplate reader (Molecular Devices, USA).

***In vitro* photothermal toxicity of nanoprobes.**

Photothermal toxicity of targeted and non-targeted nanoprobe was evaluated using both qualitative and quantitative methods. First, the HepG2 cells were cultured in 96-well plates under the same conditions as described in the above section **Cell viability**. After being treated with both nanoprobe at various doses (0, 6.25, 12.5, 25, 50, and 100 µg mL^{-1}), HepG2 cells were exposed

to a 1064 nm laser (1 W cm^{-2}) for 10 min. Quantitative analysis of *in vitro* PTT performance was obtained from a standard MTT assay.

Afterward, qualitative observation of nanoprobes' photothermal toxicity was acquired by live/dead staining. The HepG2 cells were seeded in confocal dishes at a density of 1 × 10^5 cells per dish, and divided into 7 groups: HepG2 cells treated with PBS and targeted or non-targeted nanoprobe (with and without 1064 nm laser irradiation). The cells in irradiation group received 1064 nm laser illumination (1 W cm^{-2}) for 10 min and then incubated in dark for 4 h. Subsequently, all cells were co-stained with calcein acetoxymethyl ester (calcein-AM) and propidium iodide (PI) for 30 min. These samples were imaged on a fluorescence microscope (Nikon, TE2000) to intuitively show the *in vitro* PTT efficiency of targeted and non-targeted nanoprobe against HepG2 cells intuitively.

In vitro PAI of targeted nanoprobe.

PAI was performed using a lab-built photoacoustic computed tomography (PACT) system.[22, 49, 50] The details of the PACT system are provided in the Supplementary Information (Fig. S2, ESI†). First, the PA spectrum of targeted nanoprobe was evaluated with continuous laser illumination, ranging from 650 to 1100 nm at a spectrum interval of 50 nm. PA signals of targeted nanoprobe at 1064 nm were further examined at different concentrations. Second, the targeted nanoprobe was exposed to different pulsed excitations (0-25,000 pulses) at 1064 nm to assess its photostability. Third, to investigate the deep tissue imaging capability of targeted nanoprobe, we evaluated the PA amplitude of targeted nanoprobe covered by chicken breast tissue of various thicknesses under 825 and 1064 nm laser irradiation.

In vivo PAI of animal models.

For *in vivo* PAI, targeted or non-targeted nanoprobe (250 µg mL^{-1}) was injected into orthotopic HCC-bearing mice and the LC mouse model at a dosage of 2.5 mg kg^{-1} through the tail vein. Mice were anesthetized with isoflurane (1-1.5% v/v) during the *in vivo* experiment. PA images of the liver region were acquired at different time points (preinjection, 1, 2, 3, 6, 9, 12, and 24 h postinjection). Each image was capture under the same parameters through PACT system. The excitation wavelength of 1064 nm was used for the *in vivo* PAI.

Ex vivo PAI.

The biodistribution and metabolism of targeted nanoprobe in HCC-bearing nude mice was further determined by *ex vivo* PA signal quantification with PACT system (λ_{ex} = 1064 nm). The tumors and major organs (heart, liver, spleen, lungs, and kidneys) were collected to explore the distribution at the peak time confirmed by *in vivo* PAI. Besides, to determine the metabolism of targeted nanoprobe, the *ex vivo* PAI was performed at different time (24, 36, and 48 h) post-injection of nanoprobe, while the mice receiving same volume of PBS injection were used as control to acquire the basic PA signals of major viscera.

T$_2$-weighted MRI.

MRI was conducted using a 1.0 T small animal MRI scanner (ICON, Bruker, Germany). For *in vitro* MRI, T$_2$-weighted contrast enhancement of targeted nanoprobe in Eppendorf (EP) tubes was evaluated by T$_2$-map RARE sequence, and then the transverse relaxation rate (R2) was calculated by linear fitting $1/T_2$ (s^{-1}) versus iron concentrations (mM).

After injection of targeted nanoprobe through the mouse tail vein, the T$_2$-weighted imaging of HCC and LC mice was performed preinjection and at 3 h postinjection, with the following parameters: TR/TE: 1800 ms/65 ms; averages: 8; slice thickness: 1.5 mm, FOV: 3.0 cm × 3.0 cm; matrix: 96 × 96.

PTT of orthotopic HCC *in vivo* and follow-up.

Early HCC xenografted mice with equivalent bioluminescence values were randomly divided into 4 groups with three animals per group, namely, one treatment group (targeted nanoprobe + 1064 nm laser) and three control groups (PBS only, PBS + 1064 nm laser, and targeted nanoprobe only). At 3 h postinjection of PBS (200 µL) or targeted nanoprobe (250 µg mL^{-1}, 2.5 mg kg^{-1}) through the tail vein, the mouse skin above the tumor region was exposed to the 1064 nm laser illumination (1 W cm^{-2}) for 9 min under the guidance of MRI/NIR-II PAI. The temperature evolution and infrared thermal images were recorded during PTT using an infrared thermal camera (FLIR One Pro, USA). After various treatments, tumor progression was evaluated by bioluminescence imaging and histological examination to assess the therapeutic effects. The body weight and vital signs of all mice were monitored during the 16-day follow-up.

Histological examination.

To evaluate the therapeutic efficacy and biosafety of targeted nanoprobe *in vivo*, the mice from different groups were sacrificed after follow-up and the major organs were collected for histological examination. All excised tissues fixed with formalin solution were embedded in paraffin and subsequently sectioned into 5-µm-thick slices for hematoxylin and eosin (H&E) staining.

Statistical analysis.

The data of MRI and PAI (OR-PAM and PACT) were processed and analyzed using MATLAB (R2019b. MathWorks, U.S.A.). Other data analysis was conducted with GraphPad Prism (Prism 8, Calif, USA). The measurement data are presented as the means ± standard deviation (SD) from three replicative samples.

Results and discussion

Synthesis of targeted nanoprobe

To obtain the HCC-specific contrast agent, the novel GPC-3-targeted nanoprobe was fabricated *via* following three steps. First, hydrophobic MNPs and NIR-II absorbing SP were synthesized through approaches described in the Supplementary Information, which served as the signal sources for MRI and NIR-II PAI/PTT, respectively. The hydrophobic MNPs were characterized by uniform spherical morphology with an average diameter of ~9 nm (Fig. S4, ESI†). The broad absorption band extending to the NIR-II region of
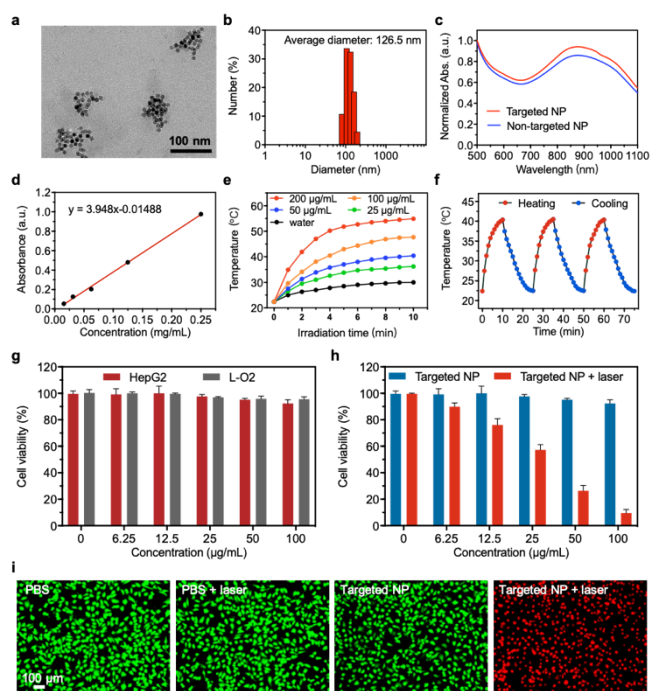
Fig. 1. Characterization of the targeted nanoprobe in morphology, optical properties, photothermal performance and toxicity. (**a**) TEM image of targeted nanoprobe. (**b**) Diameter distribution of targeted nanoprobe. (**c**) Absorption profile of non-targeted and targeted nanoprobe aqueous dispersion. (**d**) The absorption value of targeted nanoprobe at 1064 nm as a function of concentration. Red line: linear fitting. (**e**) The photothermal performance of targeted nanoprobe at different concentrations under continuous 1064 nm laser illumination (1 W cm^{-2}) for 10 min. (**f**) Photothermal stability of targeted nanoprobe (50 µg mL^{-1}) upon NIR-II irradiation (1 W cm^{-2}) for three laser on/off cycles. (**g**) MTT assay results of HepG2 and L-O2 cells incubated with targeted nanoprobe at different concentrations. (**h**) The *in vitro* PTT of HepG2 cells treated with different concentrations of targeted nanoprobe with and without 1064 nm laser irradiation (1W cm^{-2}). (**i**) Live/dead staining of HepG2 cells after treatments of PBS only, PBS + 1064 nm laser, targeted nanoprobe only, and targeted nanoprobe + 1064 nm laser. Scale bar: 100 µm.

the obtained SP (Fig. S5, ESI†) indicates the successful coupling between the two initial monomers (Fig. S3, ESI†). Second, water-dispersed nanoparticles MNP-SP@PEG (non-targeted nanoprobe) were were prepared *via* a nanoprecipitation method using SP, MNPs, and DSPE-PEG-COOH (Supplementary Information). Thus, the organic-inorganic hybrid nanoparticle was fabricated with combining beneficial characteristics of both nanocomposites.[51] Third, the HCC-targeted nanoprobe was obtained by surface modification of non-targeted nanoprobe using an anti-GPC-3 antibody (Supplementary Information).

Characterization of the nanoprobes

The basic morphological and optical characteristics of the synthesized nanoprobes were fully tested. The targeted nanoprobe presents uniformed nano-aggregates (Fig. 1a) with an average hydrodynamic diameter of 126.5 ± 4.8 nm in aqueous solution (Fig. 1b), which is slightly larger than that of non-targeted nanoprobe (Fig. S6a, ESI†), resulting from the antibody coupled to the nanoparticle surface. The nanoparticle sizes of both targeted and non-targeted

nanoprobes suspended in phosphate-buffered saline (PBS) (Fig. S6b, ESI†) and FBS (Fig. S6c, ESI†) remained almost unchanged after storage in aqueous media for one month, indicating the excellent long-term structural stability of our nanoprobes. The optical properties of targeted and non-targeted nanoprobes were investigated by measuring their absorption spectra in aqueous dispersion, and our nanoprobes showed superior imaging performance in the NIR-II region (Fig. 1c). Furthermore, a high mass extinction coefficient of 3.948 cm^{-1}mg^{-1}mL was calculated from the linear fitting of the data (Fig. 1d and Fig. S7a, ESI†), demonstrating the promising potential of targeted nanoprobe for NIR-II PAI and PTT at 1064 nm. In addition, the absorbance of targeted and non-targeted nanoprobes at 1064 nm remained almost invariable under continuous laser irradiation (10 mJ cm^{-2}) for 20 min (Fig. S7b and 7c, ESI†), which indicates the high photostability of nanoprobes.

In vitro photothermal performance of the nanoprobes

The photothermal performance of the nanoprobes was subsequently measured *in vitro*. Both targeted and non-targeted nanoprobes in this study show strong optical absorption in the NIR-II window. Therefore, the photothermal performance of nanoprobes triggered by 1064 nm laser irradiation (1 W cm^{-2}) was explored *in vitro*. A concentration-dependent temperature increase was observed in targeted and non-targeted nanoprobes solutions after laser irradiation for 10 min, whereas deionized (DI) water as a control exhibited negligible temperature elevation under the same excitation conditions (Fig. 1e and Fig. S8a, ESI†). High-temperature hyperthermia (more than 50 °C) could be easily reached, even at a low concentration of 200 µg mL^{-1}, which implies the great potential of both nanoprobes for *in vivo* PTT. Moreover, the photothermal stability of targeted and non-targeted nanoprobes was investigated by monitoring the sample temperature changes during three laser on/off cycles. The experimental results demonstrated that both nanoprobes exhibited minimal temperature change (<10%) in each "heating-cooling" cycle (Fig. 1f and Fig. S8b, ESI†), revealing the stable photosensitivity of targeted and non-targeted nanoprobes after long term NIR-II excitation. In addition, based on the previously reported equations and obtained data,[46,47] the photothermal conversion efficiency (PCE) of the targeted nanoprobe dispersion (100 µg mL^{-1}) was calculated to be 74.6% (Fig. S8c, 8d, 8e and 8f, ESI†), and the Fe$_3$O$_4$ plus SPs all contributed to the superior photothermal performance, which is equivalent to or even higher than most of other conventional organic and inorganic materials in the NIR-II window.[23,52,53] All these data illustrate the excellent photothermal and photobleach-resistant ability of targeted nanoprobe. Therefore, targeted nanoprobe represents an efficient PTA for further *in vivo* PAI and tumor therapy.

Cytotoxicity of the nanoprobes *in vitro*

To provide evidence for the biosafety applications, the dose-dependent cytotoxicity of targeted and non-targeted nanoprobes *in vitro* was studied by testing the cell viability using the standard MTT assay method. After incubation with both nanoprobes at concentrations ranging from 6.25 to 100 µg mL^{-1} for 24 h, more than 90% of Hep-G2 and L-O2 cells remained viable without NIR-II laser

exposure (Fig. 1g and Fig. S9a, ESI†), implying the negligible cytotoxicity of targeted and non-targeted nanoprobes at the cellular level.

In vitro photothermal efficiency

Moreover, the photothermal toxicity of the designed nanoprobes was also evaluate at the cellular level. HepG2 cells cultured with targeted and non-targeted nanoprobes were exposed to the 1064 nm laser irradiation (1 W cm^{-2}). According to the MTT assay results in Fig. 1h and Fig. S9b(ESI†), obvious dose-dependent destruction was observed in nanoprobe-treated HepG2 cells after NIR-II light exposure for 10 min. In particular, the cell viabilities decreased much significantly after incubation with targeted nanoprobe compared with non-targeted under 1064 nm laser illumination, which is associated with higher accumulation of targeted nanoprobe in HepG2 cells due to its active GPC-3 binding ability. Remarkably, only less than 10% of HepG2 cells (necrosis rate: 90.43%) remained alive after laser excitation at a targeted nanoprobe concentration of 100 µg mL^{-1}, indicating the excellent photohyperthermic effects of targeted nanoprobe on HepG2 cells.

In addition, to qualitatively visualize the photoablation performance of targeted and non-targeted nanoprobes, the HepG2 cells were stained with a live/dead kit after receiving diverse treatments (PBS only, PBS + NIR-II laser, nanoprobes only, and nanoprobes + NIR-II laser) (Fig. 1i and Fig. S9c, ESI†). Red fluorescence was only present in the groups of HepG2 cells administrated the nanoprobes + NIR-II laser treatment (Fig. 1i and Fig. S9c, ESI†), illustrating that 1064 nm laser irradiation combined with both nanoprobes can induce the destruction of HepG2 cells. Importantly, the red fluorescence region was much larger when incubated with targeted nanoprobe than non-targeted nanoprobe, suggesting that HepG2 cells take up more targeted nanoprobe than non-targeted one at the same concentration, which was consistent with the quantitative MTT assay results. Besides, the green fluorescence in other groups (Figure 1i, Figure S9c) also demonstrated that NIR-II laser irradiation or nanoprobes alone had little effect on cell viability, which validated the safe experimental dose of either 1064 nm laser radiation or the nanoprobe itself. These data provided solid evidence that targeted nanoprobe could be used as an effective PTA for ablation of early-stage HCC in the combination with 1064 nm laser illumination.

Photoacoustic characterization of the targeted nanoprobe

Inspired by the high PCE of nanoprobes in NIR-II window, we further assessed the performance of targeted nanoprobe as NIR-II PAI contrast agent using a lab-built PACT system. First, when investigating the PAI window of targeted nanoprobe, the PA spectrum of targeted nanoprobe as illustrated in Figure 2b is consistent with the absorption profile, and a strong PA signal was achieved at 1064 nm (energy intensity: 10 mJ cm^{-2}). The targeted nanoprobe also exhibited good linear relationships between the PA amplitude at 1064 nm and increased concentrations (Fig. 2a and 2c), indicating the feasibility of quantitative PA imaging within the NIR-II window. In addition, the PA amplitude of targeted nanoprobe
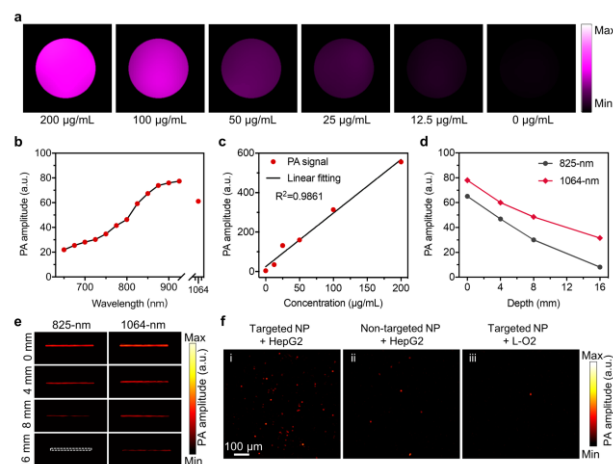

Fig. 2. Photoacoustic characterization of the targeted nanoprobe. (**a**) PA images of targeted nanoprobe dispersions at different concentrations under 1064 nm laser irradiation. (**b**) PA spectrum of targeted nanoprobe (250 µg mL^{-1}) aqueous dispersion. (**c**) Linear fitting of normalized PA amplitude at 1064 nm of targeted nanoprobe as a function of concentrations. (**d**) The corresponding normalized PA amplitude of targeted nanoprobe excited by 825 nm or 1064 nm laser irradiation at different depths. (**e**) PA images of targeted nanoprobe aqueous dispersion (250 µg mL^{-1}) embedded in chicken breast tissue of various thicknesses under both NIR-I (825 nm) and NIR-II (1064 nm) laser illumination (laser energy: 10 mJ cm^{-2}). (**f**) Targeting ability of targeted nanoprobe in vitro scanned by OR-PAM. The PA images of HepG2 (i) and L-O2 (iii) cells incubated with targeted nanoprobe, as well as the HepG2 cells incubated with non-targeted nanoprobe (ii) at the same concentrations (50 µg mL^{-1}) for 12 h. (excitation wavelength: 532 nm, pulse energy: 75 nJ). Scale bar: 100 µm.

displayed few fluctuations, even after excitation with 25,000 pulses of a 1064 nm laser (Fig. S7d, ESI†), which reveals the superior photostability of targeted nanoprobe for long-term imaging tasks. Moreover, to testify the deep imaging ability of targeted nanoprobe in the NIR optical window, the PA signals at different imaging depths were measured and compared both in NIR-I (825 nm) and NIR-II (1064 nm) windows (Fig. 2d and 2e). The PA amplitude decreased gradually with the increasing thickness of covered chicken breast tissue from 4 to 16 mm at both wavelengths. However, the NIR-II PAI always exhibited stronger signals than NIR-I PAI at the same depth and concentration of targeted nanoprobe. For instance, although it is barely possible to detect the PA signal at 825 nm when the imaging depth is 16 mm, NIR-II PAI can still display the signal of the targeted nanoprobe sample clearly. These results confirm the superiority of targeted nanoprobe for deep tissue imaging, making it a promising candidate for NIR-II light-mediated theranostics of orthotopic HCC at in vivo depths.

The in vitro HCC-targeting properties of nanoprobes

The GPC-3 receptor-specific binding ability of targeted nanoprobe in vitro was assessed and analyzed via OR-PAM imaging. HCC is a highly malignant tumor with high expression of GPC-3 on the cell membrane of human HCC cell lines, but is absent in human normal hepatic cells and cirrhotic tissue. OR-PAM can identify the PA signals emitted by nanoprobes bound to the cytomembrane due to the extremely high accuracy and

resolution (2μm-5μm) of this method,[54] which is beneficial for sensitively exploring the *in vitro* active targeting of nanoprobes. After incubating HepG2 and L-O2 cells with nanoprobes, the OR-PAM scanning of Petri dishes was performed. The maximum amplitude projection along the depth direction (MAP) images revealed that anti-GPC-3 antibody-containing targeted nanoprobe can bind to the HepG2 cell membrane actively and emit strong PA signals (Fig. 2f (i)), validating its specific targeting to GPC-3. Notably, although the binding of non-targeted nanoprobe was observed in HepG2 cells (Fig. 2f (ii)), the PA amplitude was much lower, which may be attributed to the passive uptake of non-targeted nanoprobe by tumor cells. In contrast, targeted nanoprobe-treated L-O2 cells displayed inconspicuous PA signals (Fig. 2f (iii)), showing that little targeted nanoprobe was bound to L-O2 cells since no GPC-3 expression existed in nontumorous or normal adult liver tissue.

Corresponding quantitative analysis also showed that the PA intensity of targeted nanoprobe in HepG2 cells was ~5.6-fold and ~298.3-fold stronger than that of non-targeted nanoprobe-treated HepG2 cells and targeted nanoprobe-treated L-O2 cells, respectively (Fig. S10, ESI†). These phenomena demonstrated the preferential accumulation of targeted nanoprobe to HepG2 cells with GPC-3 overexpression, validating the high HCC-specific binding of targeted nanoprobe for further precisely theranostic applications.

In vivo real-time PAI and the diagnosis of micro-HCC based on targeted nanoprobe

Generally, the orthotopic HCC model showed much similar tumor microenvironment to human liver cancer in respect of vascular supply, biological behavior, and tumor progression, which is more suitable for theranostic study of HCC than conventional subcutaneous tumor model.[55] Based on the *in vitro* imaging results, the real-time NIR-II PAI was performed to visualize the *in vivo* tumor-specific accumulation of targeted nanoprobe and diagnostic accuracy to orthotopic early HCC through a lab-built PACT system. The PACT system can achieve real-time macroscopic imaging *in vivo* with penetration depths greater than 3-5 cm, which is beneficial to perform accurate and sensitive cross-sectional imaging for tumor diagnosis.[56]

After confirming the formation of orthotopic micro-HCC *via* bioluminescence imaging, the tumor-xenografted mice were selected with equivalent bioluminescence values to ensure similar tumor sizes. The targeted and non-targeted nanoprobe (250 μg mL^{-1}, 2.5 mg kg^{-1}) were separately injected into two groups of tumor-bearing mice intravenously, PA images were obtained prior to injection and at different time intervals (1, 2, 3, 6, 9, 12, and 24 h) postinjection to monitor the accumulation of nanoprobes in micro-HCC *in vivo*. The cross-sectional images showed that the PA amplitude of the liver in both groups increased rapidly over time after injecting nanoprobes. Benefiting from the accumulation of nanoprobes in HCC, the PA signals of the tiny tumor regions presented a time-dependent increase and reached the peak value at about 3 h postinjection. Then all signals decreased and almost returned to baseline at about 24 h (Fig. 3a and 3b). The depth of HCC was

approximately 4 mm under the skin abdomen. In addition, although PA amplitude in both groups showed a similar peak time and trend, the further quantitative analysis demonstrated that a stronger PA signal of HCC was observed in mice treated with the targeted nanoprobe at similar tumor sizes and locations (Fig. 3d and 3e). Especially at 3 h after systemic administration of targeted nanoprobe, the PA signal enhancement of tumor was 14.5-fold greater than that of the baseline. In general, the non-targeted nanoparticles aggregate at tumor sites due to the enhanced permeability and retention (EPR) effect in a passive targeting manner.[57] But some early-stage tumor may not exhibit the EPR effect due to regular vascular structure and tiny tumor size, and it is also controversial whether EPR effect exists or not in human tumors, which limited the aggregation efficiency of non-targeted nanoprobes.[33] Nevertheless, targeted nanoprobe exhibited much more accumulation in orthotopic HCC due to its active binding ability to oncogenic biomarkers expressed on the HepG2 cytomembrane, which contributes to the higher nanoparticle retention and PA signal in GPC-3 positive HCC for better anti-cancer therapeutic effect. Thus, the targeted nanoprobe showed better prospect for practical applications, and should be used in the subsequent imaging and treatment experiments of HCC. Meanwhile, the real-time PAI also showed that the accumulation of the targeted nanoprobes in HCC reach the peak at 3 hours post-injection, demonstrating the optimal imaging time for clearest visualization and subsequent treatment of early-HCC. Consequently, the NIR-II PAI using targeted nanoprobe can discriminate orthotopic ultra-small HCCs (with a diameter as small as approximately 1.78 mm) from the surrounding normal liver tissues accurately based on its high temporospatial resolution and optical sensitivity.

Verification about HCC-specificity of targeted nanoprobe *in vivo*

In accordance with *in vitro* results of cellular binding ability, we explored the PAI characteristics of between HCC and benign liver lesion model to further confirm the active HCC-specificity of the targeted nanoprobe. Liver cirrhosis (LC) is the common benign liver disease and is the most important risk factor for HCC.[58] And it is challenging to differentiate early HCC from cirrhotic nodules using traditional imaging methods mainly based on morphological features currently.[4,6,59] Therefore, we chose LC as the representative of the benign liver disease and assess the imaging features between HCC and LC after injecting targeted nanoprobe. Upon receiving targeted nanoprobe (250 μg mL^{-1}, 2.5 mg kg^{-1}) intravenously, the PA signals in the LC increased gradually and reached the maximum at about 3 h, followed by a gradual decrease to the pre-scan level by about 24 h postinjection as well. However, both the whole liver and subcutaneous blood vessels exhibited elevated PA signals in cirrhotic mice, and the PA signal in cirrhotic liver was almost evenly distributed without significantly strong signal points (Fig. 3c and 3f). These phenomena were caused by comprehensive pathological changes in LC. LC is a chronic disease that involves the whole liver. During the progression of LC induced by CCl$_4$ ingestion, diffused inflammation and an immune response occur in the whole liver parenchyma, which cause neovascularization and increased blood
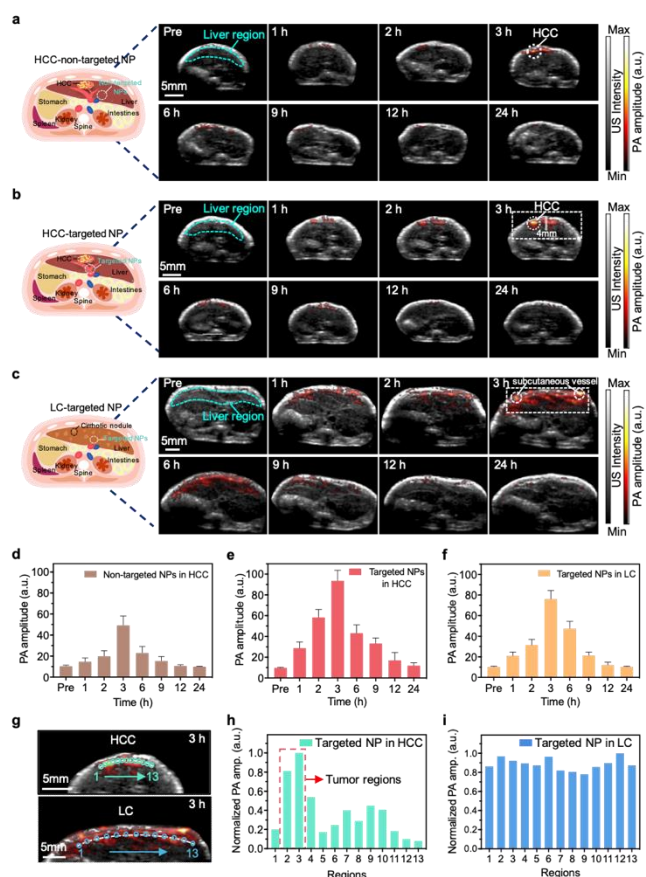
Fig. 3. *In vivo* **real-time PAI and quantitative analysis of orthotopic early-stage HCC.** The schematic diagram, merged ultrasound (US, grayscale) and NIR-II PA (red-hot scale) images of orthotopic HCC treated with non-targeted nanoprobe (**a**) (250 μg mL^{-1}, 2.5 mg kg^{-1}), orthotopic HCC (**b**) and LC treated by targeted nanoprobe (**c**) (250 μg mL^{-1}, 2.5 mg kg^{-1}) at various postinjection time. The liver region is circled with the blue dotted lines based on the anatomical structure in the US image at preinjection; the HCC tumor and subcutaneous vessels in LC were circled with white dotted lines in 3 h. The evenly distributed regions (b, c) to be analyzed in (h) are enclosed with a white dotted box in 3 h. The normalized PA amplitude of HCC at different time points after injection of non-targeted nanoprobe (**d**) and targeted nanoprobe (**e**). The normalized PA amplitude of the LC (**f**) at different time points after injection of targeted nanoprobe. (**g**) The regions of interest (green and blue circles) to be analyzed for PA signals of HCC (above) and LC (below) at 3 h postinjection of targeted nanoprobe. The normalized PA amplitude of different regions in mouse liver with HCC (**h**) and cirrhotic liver (**i**). The HCC tumor region is marked by a red dotted box. λ_{ex} = 1064 nm, energy density: 14 mJ cm^{-2}, Scale bar: 5 mm.

supply in the cirrhotic liver. After injecting targeted nanoprobe, the PA amplitude of LC rises due to increased and evenly distributed nanoprobes in cirrhotic liver, which is associated with increased vascular flow and absence of GPC-3 expression in LC.[60,61] Moreover, the strong PA signal from subcutaneous vessels is attributed to elevated blood flow and dilated vessels in subcutaneous regions, which is one of the cutaneous manifestations of LC.[62-64]

In addition, although the signal changes of HCC and LC showed similar temporal trends following the targeted nanoprobe administration, the spatial distribution of PA signals

in these two pathological environments were quite different (Fig. 3b and 3c). Quantitative analysis of NIR-II PAI was carried out to further elucidate the spatial distribution characteristics of targeted nanoprobe in these two models. At 3h postinjection of targeted nanoprobe during PAI, 13 regions were randomly acquired from evenly spaced areas on the liver, and the average PA amplitude of these regions was analyzed (Fig. 3g). In tumor-xenografted mice, the PA amplitude in the HCC region was significantly higher than that in other normal liver tissues or blood vessels (Fig. 3h), indicating that targeted nanoprobe had a more obvious tendency of enrichment in orthotopic HCC due to its ability to target and bind to GPC-3 actively. By contrast, there was no significant strong-signal point in LC mice, and the dispersive PA signals only fluctuated within a small range (Fig. 3i). The spatial imaging features of NIR-II PAI were caused by the lack of GPC-3 antigen in the cirrhotic and normal liver, which weakens the recognition capability of targeted nanoprobe. Thus, the PAI results verified the HCC-specific diagnosis of targeted nanoprobe and provide potential reference for differential diagnosis of HCC and LC.

MRI for further description of orthotopic early-stage HCC

Among the current common imaging modalities, MRI is regarded as one of the most widely used imaging technique for tumor diagnosis in the clinic in terms of its superior high soft tissue contrast and spatial resolution, which is expected to have complementary advantages with PAI.[7] Furthermore, previous research revealed the great potential of MNP-enhanced T_2-weighted MRI in diagnosing HCC.[28] Thus, in accordance with the real-time diagnostic results and optimal accumulation time of the targeted nanoprobe delivered by NIR-II PAI, the performance of T_2-MRI with targeted nanoprobe was systematically assessed both *in vitro* and *in vivo.* In this way, a dual-modal imaging strategy that combines the comprehensive advantages of MRI and NIR-II PAI has great potential for the precise diagnosis of micro-HCC while showing a clear spatially adjacent relationship between the tumor and surrounding tissues or organs.

Firstly, the different concentrations of targeted nanoprobe (equivalent dose of Fe) were imaged in 1.0T MRI scanner to clarify the T_2-MR signals from MNPs. When recording the T_2-weighted MRI contrast images of targeted nanoprobe, the negative signals appeared and the darkness increased with an increasing Fe concentration (Fig. 4a). And the transverse relaxation rate (R_2) was calculated to be 130.7 mM^{-1}s^{-1} (Fig. 4b). Thus, the Fe$_3$O$_4$ NPs in our nanoprobe exhibits good superparamagnetic behavior and relaxivity, which demonstrated that the targeted nanoprobe can be used as an excellent contrast agent for T_2-weighted MRI of HCC.

After confirming the T_2-MR signal of targeted nanoprobe, the MRI was performed in nude mice bearing orthotopic early HCC. Before injecting targeted nanoprobe, it is hard to accurately distinguish the tumor from normal liver tissue due to both tissues showed similar T_2 signals (Fig. 4c pre). In comparison with preinjection MR image, the negative MR signals of tumor appeared due to significantly shortening of the T_2 relaxation at
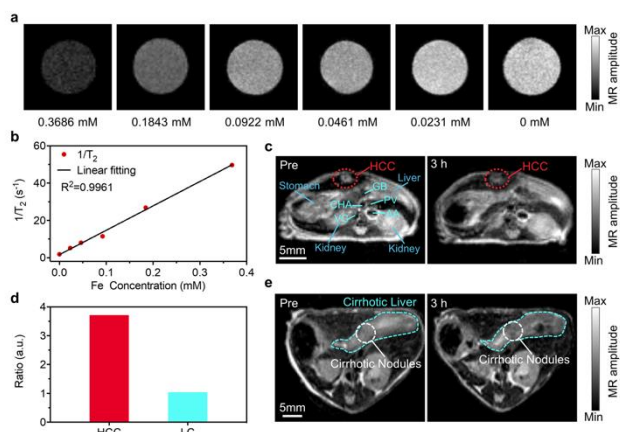
Fig. 4. *In vivo* MRI for high spatial-resolution diagnosis of early HCC at the PAI-guided optimal imaging time. (**a**) T_2-weighted MR images of different concentrations of Fe (mM). (**b**) Relaxation rates $1/T_2$ (s^{-1}) of targeted nanoprobe as a function of Fe concentrations (mM). (**c**) T_2-weighted MR images of orthotopic HCC pre- and 3 h post- injection of targeted nanoprobe intravenously (250 µg mL^{-1}, 2.5 mg kg^{-1}) in grayscale. The HCC tumor is circled with red dotted lines. GB: Gall bladder, CHA: Common hepatic artery, PV: Portal vein, AA: Abdominal aorta, VC: Vena cava. (**d**) The ratio of T_2-MR signal pre/3h in the HCC and LC. (**e**) T_2-weighted MR images of LC pre- and 3 h post-injection of targeted nanoprobe intravenously (250 µg mL^{-1}, 2.5 mg kg^{-1}) in grayscale. The liver region is circled with the blue dotted lines. The typical cirrhotic nodules were circled with white dotted lines. Scale bar: 5 mm.

3 h postinjection of targeted nanoprobe. And based on high spatial resolution and soft tissue contrast, the T_2-MR image exhibited notably dark contrast enhancement at the HCC focality compared with surrounding nontumorous liver tissue, which is favorable for tumor identification and understanding the adjacent relationship between the tumor and main vasculature (e.g., common hepatic artery, portal vein, abdominal aorta, vena cava) as well as abdominal organs (Fig. 4c 3h). In addition to identifying micro-HCC sensitively, the clear understanding of these surrounding structures also plays an important role in the determination of tumor invasion degree, staging, and grading, which is helps to make comprehensive evaluation of HCC and formulate the reasonable treatment plans. Hence the NIR-II PAI/T_2-MRI based on multifunctional targeted nanoprobe can not only delineate micro-HCC precisely, but also clearly present the main anatomical structures in the abdominal cavity to perform appropriate treatments and avoid related injuries subsequently. Therefore, it is feasible to apply targeted nanoprobe for the comprehensive and precise diagnosis of early-stage HCC via dual-modal imaging strategy, and ultimately guide the further treatment.

In addition, disparate imaging results were also observed in MRI of LC model: In the preinjection MRI image, the scattered dotted areas with slightly low T_2 signals indicated by the circles were considered as cirrhotic nodules. Then at 3 h post-administration of targeted nanoprobe, the image on the same slice showed that the T_2 signal of the whole liver was slightly reduced, but the small cirrhotic nodules were not clearly contrasted with the surrounding tissues (Fig. 4e). Furthermore,

the relative change of MRI signal in the tumor region and cirrhotic nodules were analyzed quantitatively. The ratio of the T_2 signal in the HCC region before and 3 h after injection of targeted nanoprobe in HCC region was 3.71 (the T_2 signal was reduced by 73.05% at 3 h postinjection), which presented a clear contrast between HCC and surrounding normal liver tissue. Moreover, the ratio of the T_2 signal in the LC region before and 3 h after injection of targeted nanoprobe in LC was 1.04 (the T_2 signal was reduced by 3.85% at 3 h postinjection) without significantly targeted accumulation into the cirrhotic nodules (Fig. 4d). The MRI results were caused by different spatial distribution of targeted nanoprobe, which is associated with significantly higher GPC-3 intensity in HCC than in nontumorous liver tissue. All the above imaging results of HCC and LC were confirmed by histological examinations (Fig. S11, ESI†). These findings not only validate the effectiveness of targeted nanoprobe as HCC-targeted contrast agent for dual-modal imaging, but also indicate its potential to differentiate micro-HCC from LC through their divergent imaging characteristics.

Collectively, the above NIR-II PAI/T_2-MRI results indicate that the targeted nanoprobe holds great promise for HCC-specific targeted accumulation and as an effective contrast agent for multimodal imaging. Although NIR-II PAI provide specific information of micro-HCC in real time with a high sensitivity and temporospatial resolution at the tumor region, it remains unsuitable to visualize some main anatomical structures in deep tissue clearly within abdominal cavity. Despite of unsatisfactory temporal resolution and imaging sensitivity, MRI can offer details about spatially adjacent relationship between the tumor and surrounding structures (e.g., tissues, vessels, bile ducts and organs) without the penetration depth limitation. Hence, it is of great value to combining these two imaging modalities to overcome their respective limitations. Consequently, the dual-modal NIR-II PAI/T_2-MRI using targeted nanoprobe could afford targeted and complementary imaging information about orthotopic early HCC *in vivo*, which is beneficial to the precise and comprehensive diagnosis plus radical treatment of early-stage HCC especially in high-risk patients.

The biodistribution of the targeted nanoprobe at peak time

Besides, the biodistribution of the targeted nanoprobe was further investigated through NIR-II PAI. In general, the application of nanoprobes in practice is often limited by inefficient aggregation in lesions.[65] In order to verify the targeted accumulation of this targeted nanoprobe, the HCC-bearing mice were sacrificed after 3h postinjection, and the major viscera (heart, liver, spleen, lungs, and kidneys) including tumor tissue were collected to further analyze the distribution of PA signals. At 3h postinjection of targeted nanoprobe, the *ex vivo* analysis showed that the tumor exhibited the strongest PA signal, followed by the liver, spleen, and other organs (Fig. 5a and 5b). The low-level PA signal in the liver and spleen is associated with a small quantity uptake of nanoparticles by the reticuloendothelial system (RES) within the liver and spleen.[66] The strongest PA signals in HCC demonstrated the efficient aggregation of targeted nanoprobes in the tumor based on its pronounced active molecular specificity to HCC due to the GPC-3-mediated receptor-antibody

interaction, which is beneficial to enhanced theranostic effects *in vivo* and will minimizes the impact on noncancerous liver.
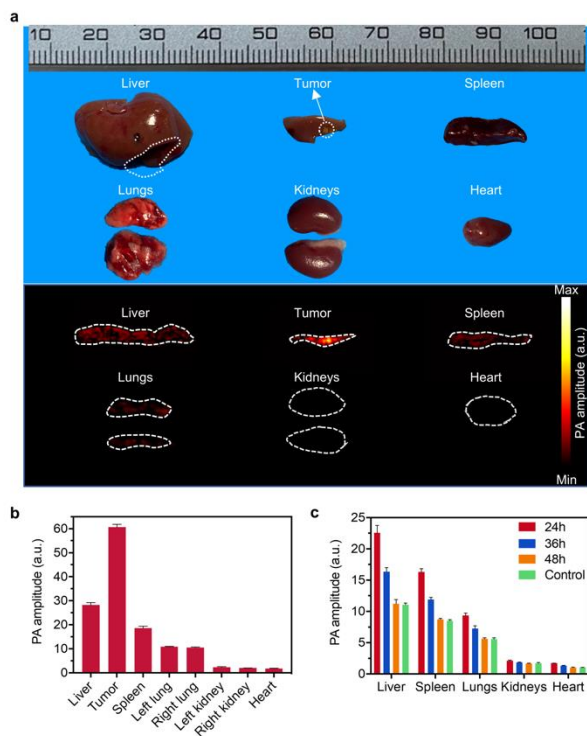

Fig. 5. Metabolism and biodistribution of the targeted nanoprobe in orthotopic HCC mouse model. (**a**) Overlapping images of *ex vivo* PA signals (λ = 1064 nm) from organs' cross-sections (lower row) and actual organs (upper row) at 3 h post-injection of targeted nanoprobe (250 µg mL^{-1}, 2.5 mg kg^{-1}). The white dotted area in liver is the location of liver part including tumor. (**b**) Quantitative analysis of *ex vivo* PA signals from tumor and major organs in (a); (**c**) PA signals of the ex vivo organs (λ = 1064 nm) excised from mice at control groups as well as at 24 h, 36 h, and 48 h post-injection of targeted nanoprobe (250 µg mL^{-1}, 2.5 mg kg^{-1}).

The metabolism of the targeted nanoprobe

Furthermore, the *in vivo* accumulation of nanoparticles still raises health concerns about their toxicity and safety for human.[65] Thus, the major organs of mice were collected at 24, 36, 48 h postinjection to evaluate the metabolism of targeted nanoprobe *in vivo*. And the mice receiving same volume of PBS injection were used as control to understand the basic PA amplitude of major viscera. The metabolism study of targeted nanoprobe showed that the PA amplitude from all organs faded gradually after 24 h and almost completely vanished at 2 days post-administration in comparison with control group (Fig. 5c). Such a distribution pattern and metabolic trend also manifested the predominant hepatobiliary clearance process of targeted nanoprobe *in vivo*.[67] The *ex vivo* PAI results present the minimal accumulation of nanoprobe in body, reinforcing the biosafety of this organic-inorganic hybrid targeted nanoprobe for *in vivo* application.

Non-invasive photothermal treatment of orthotopic early-stage HCC

In patients with early HCC, multiple randomized controlled trials to date have demonstrated the similar or improved disease-free survival and overall survival after ablation compared with hepatectomy, while the trauma and severe complications are less in patients receiving ablation. Thus, the ablation has been considered as the first-line treatment in HCC patients with BCLC stage 0 and A.[17,18] However, the commonly used ablation methods still involve certain trauma and injuries to the normal tissues around the tumor.[19,68] As a new type of ablation treatment, the non-invasive NIR-II PTT with high selectivity and deep penetration is promising for achieving satisfactory therapeutic outcomes in early-stage HCC.

In this study, the schematic diagram of imaging-guided PTT and follow-up is presented in Fig. 6a. Based on the guidance NIR-II PAI/T$_2$-MRI, the optimal therapeutic range and time was determined before treatment. The targeted nanoprobe (250 µg mL^{-1}, 2.5 mg kg^{-1}) or 200 µL PBS was injected into tumor-bearing mice with HepG2 xenografts intravenously. Then at fixed time points (days 1, 3, and 5) after 3h postinjection, the mouse skin above the tumor region was kept intact and exposed to 1064 nm laser irradiation (1 W cm^{-2}) (Fig. 6a, Fig. S12, ESI†). In the treatment group, the local skin temperature above the tumor area reached a maximum temperature plateau of 50.6 °C within 5 min, which exceeded the temperature threshold (43 °C) for the ablation of tumor.[69] And the PTT was maintained until 9 min for adequate HCC ablation because additional hyperthermia of high temperature (> 50 °C for 4-6 min) was sufficient to induce irreversible damage to the tumor. Meanwhile, a mild thermal elevation (maximum temperature is 42.8 °C) was observed from the surrounding tissues.[65] The different temperatures between tumor and adjacent tissue could be attributed that the targeted nanoprobe could bind to HCC specifically and promote great enrichment at tumor region, avoiding damage to disease-free liver tissues (Fig. 6b and 6c).[70] In contrast, the mice treated with PBS did not exhibit an appreciable temperature increase, and the final maintained temperature was less than 40 °C under the same irradiation conditions (Fig. 6b and 6c). The distinct temperature elevation not only confirms the safety of the laser power selected in this study, but also indicates that the local photothermal effect was benefited from the combination of targeted nanoprobe and NIR-II laser irradiation.

The follow-up and treatment evaluation

After finishing the course of treatment, none of thermal damage was found in control groups. While two days after PTT, a mild scorch derived from local hyperthermia could be observed at the irradiated site in the mice from the treatment group; then the skin of the illuminated area returned to normal with no lesion remaining after the eschar fell off, suggesting that non-invasive PTT was associated with minimal side effects and excellent biosafety. Furthermore, the body weight of all mice was monitored every other day for 16 days, and there were no apparent changes among all mice in terms of body weight and vital signs during surveillance (Fig. 6e), indicating that the dose of nanoprobe in this study is well-tolerated.

During the 16-day follow-up period, the bioluminescence imaging was employed to check the therapeutic effect of non-invasive PTT against orthotopic micro-HCC *in vivo*. The

bioluminescence dramatically decreased in the treatment group, exhibiting the excellent tumor inhibition without recurrence after non-invasive PTT. By contrast,
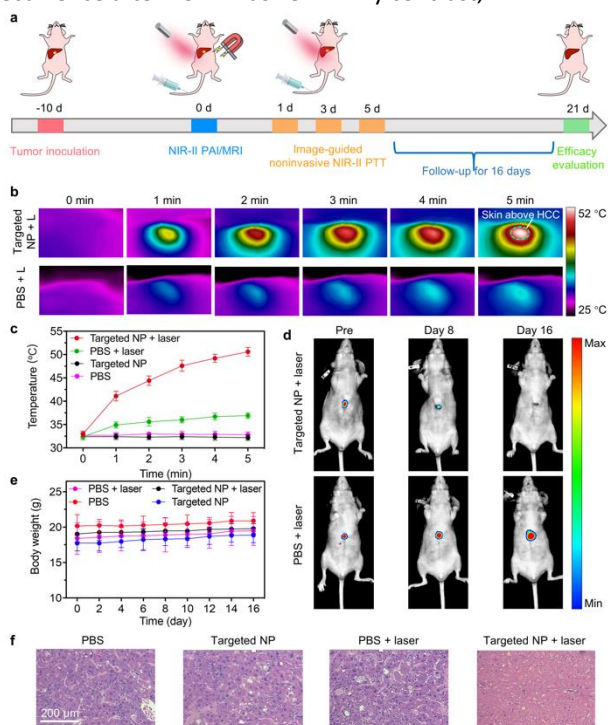

Fig. 6. Non-invasive photothermal treatment of orthotopic early-stage HCC. (**a**) Schematic illustration of image-guided non-invasive NIR-II PTT of early orthotopic HCC. (**b**)Infrared thermal images of orthotopic HCC-bearing mice treated with PBS (200 µL) and targeted nanoprobe (250 µg mL^{-1}, 2.5 mg kg^{-1}) in the first 5 min of temperature-rise period during PTT (λ_{ex} = 1064 nm, 1 W cm^{-2}). (**c**) Temperature changes in HCC bearing mice receiving different treatments. (**d**) Bioluminescence images of mice in the targeted nanoprobe + laser (upper) and PBS + laser group (lower). (**e**) Body weight change of mice from different groups during the follow-up period. (**f**) Histological examination of the tumors from different groups. Scale bar: 200 µm.

bioluminescence imaging showed that there was no tumor suppression was found in the control groups compared with that of the original status (Fig. 6d), indicating that the synergistic therapeutic effect of targeted nanoprobe and simple 1064 nm laser irradiation exhibited significant tumor-suppression.

In addition, the histological examinations were performed to further verify the tumor deterioration after PTT and the potential long-term *in vivo* toxicities of targeted nanoprobe after surveillance. The standard H&E staining plates showed severe cell necrosis and thorough tumor eradication wrapped by fibrous tissue in the treatment group, while the significant malignant proliferation was observed in the control groups. (Fig. 6f). Moreover, when analyzing the major organs (heart, liver, spleen, lung, and kidney) from all groups, there is no apparent abnormality, pathological damages, cell apoptosis or necrosis in all mice after receiving various treatments (Fig. S13, ESI†), indicating that the targeted PTT is specific to tumors and that targeted nanoprobe has ideal biocompatibility at the tested dosage at both the cellular and tissue levels.[71]

Although some previous studies have already performed invasive or minimal-invasive PTT for orthotopic HCC *via* laparotomy or laparoscopy,[43,44] our non-invasive PTT based on complementary dual-modal imaging and HCC-targeted nanoprobe also achieved satisfactory anti-tumor effects with negligible systemic toxicity, which present great effectiveness and prospects for specific, non-invasive, and safe theranostics of early-stage orthotopic HCC in clinical application. The successful non-invasive PTT in this study might be attributed to the following mechanisms: (1) the PEG encapsulation of nanoprobe improves the *in vivo* circulation stability; (2) the dual-modal imaging determined the optimal therapeutic range and time; (3) the active binding method promotes the GPC-3-specific nano-system targets to HepG2 cells *via* receptor-ligand interaction, which increases the accumulation efficiency of nano-system into HCC; (4) the combination of targeted nanoprobe and 1064 nm laser irradiation play important role in the non-invasive PTT of orthotopic HCC.

Conclusions

In summary, this study developed a novel GPC-3-targeted nanoprobe for early-stage HCC theranostics based on NIR-II PAI/T$_2$-MRI, and finally guided the non-invasive PTT of orthotopic micro-HCC. The targeted organic-inorganic hybrid nano-system exhibits excellent dual-modal imaging capacity, reliable biocompatibility and a high PCE under 1064 nm light irradiation, showing excellent GPC-3 targeting efficiency in micro-HCC with rapid accumulation and significant clearance. With the synergistic advantages of NIR-II PAI/T$_2$-MRI and HCC-targeted nanoprobe, this new diagnostic strategy can not only monitor the tumors and nanoprobes targeting process in real-time, but also delineate the comprehensive information of micro-HCC precisely with high tumor-to-normal contrast at the best imaging time based on excellent temporospatial resolution and optical sensitivity. In addition, the non-invasive PAI-guided PTT was performed against orthotopic early-stage HCC with satisfactory antitumor efficacy and little nonspecific damage to normal hepatic tissue in murine model. This study not only provides a novel and promising diagnostic strategy based on HCC-targeted multifunctional nanoprobe and dual-modal NIR-II PAI/T$_2$-MRI against early-stage HCC, but also offers non-invasive PTT to orthotopic tumors in deep tissue, which shed light on development of precise nanotheranostics of early-stage HCC and improve the prognosis of patients at risk.

Conflicts of interest

There are no conflicts to declare.

Acknowledgements

Notes and references

1   R. L. Siegel, K. D. Miller and A. Jemal, 2020, *CA Cancer J. Clin.*, 2020, **70**, 7-30.
2   N. Fujiwara, S. L. Friedman, N. Goossens and Y. Hoshida, *J. Hepatol.*, 2018, **68**, 526-549.
3   A. Villanueva, *N. Engl. J. Med.*, 2019, **380**, 1450-1462.
4   A. M. Covey, *J. Natl. Compr. Canc. Netw.*, 2018, **16**, 663-665.
5   H. Wu, M. D. Wang, L. Liang, H. Xing, C. W. Zhang, F. Shen, D. S. Huang and T. Yang, *Small*, 2021, **17**, e2005236.
6   A. Forner, M. Reig and J. Bruix, *Lancet*, 2018, **391**, 1301-1314.
7   S. Kim, J. An, Y. Lim, S. Han, J. Lee, J. Byun, H. Won, S. Lee, H. Lee and Y. Lee, *JAMA Oncol.*, 2017, **3**, 456-463.
8   Y. Tsukahara, Y. Okajima, A. Yamada, M. Momose, T. Uehara, A. Shimizu, Y. Soejima and Y. Fujinaga, *World J. Surg. Oncol.*, 2021, **19**, 41.
9   R. Weissleder and M. Pittet, *Nature*, 2008, **452**, 580-589.
10 L. Wang and S. Hu, *Science*, 2012, **335**, 1458-1462.
11 P. Zhang, L. Li, L. Lin, J. Shi and L. Wang, *Light Sci. Appl.,* 2019, **8**, 36.
12 A. Smith, M. Mancini and S. Nie, *Nat. Nanotechnol.*, 2009, **4**, 710-711.
13 M. Zha, X. Lin, J. S. Ni, Y. Li, Y. Zhang, X. Zhang, L. Wang and K. Li, *Angew. Chem. Int. Ed. Engl.*, 2020, **59**, 23268-23276.
14 X. Zhang, L. An, Q. Tian, J. Lin and S. Yang, *J. Mater. Chem. B*, 2020, **8**, 4738-4747.
15 Y. Ren, S. He, L. Huttad, M. S. Chua, S. K. So, Q. Guo and Z. Cheng, *Nanoscale*, 2020, **12**, 11510-11517.
16 Q. Fu, Z. Li, J. Ye, Z. Li, F. Fu, S. Lin, C. Chang, H. Yang and J. Song, *Theranostics*, 2020, **10**, 4997-5010.
17 J. Heimbach, L. Kulik, R. Finn, C. Sirlin, M. Abecassis, L. Roberts, A. Zhu, M. Murad and J. Marrero, *Hepatology,* 2018, **67**, 358-380.
18 European Association for the Study of the Liver, *J. Hepatol.*, 2018, **69**, 182-236.
19 J. D. Yang and J. K. Heimbach, *BMJ*, 2020, **371**, m3544.
20 B. Guo, Z. Sheng, D. Hu, C. Liu, H. Zheng and B. Liu, *Adv. Mater.*, 2018, **30**, e1802591.
21 L. Wu, W. Xie, H. M. Zan, Z. Liu, G. Wang, Y. Wang, W. Liu and W. Dong, *J. Mater. Chem. B*, 2020, **8**, 4648-4659.
22 S. Li, Q. Deng, Y. Zhang, X. Li, G. Wen, X. Cui, Y. Wan, Y. Huang, J. Chen, Z. Liu, L. Wang and C. Lee, *Adv. Mater.*, 2020, **32**, e2001146.
23 Y. Liu, P. Bhattarai, Z. Dai and X. Chen, *Chem. Soc. Rev.*, 2019, **48**, 2053-2108.
24 Y. Chen, B. Sun, X. Jiang, Z. Yuan, S. Chen, P. Sun, Q. Fan and W. Huang, *J. Mate. Chem. B*, 2021, **9**, 1002-1008.
25 M. Xie, Y. Zhu, S. Xu, G. Xu, R. Xiong, X. Sun and C. Liu, *Nanoscale*, 2020, **12**, 11497-11509.
26 S. Chatterjee, X. S. Li, F. Liang and Y. W. Yang, *Small*, 2019, **15**, e1904569.
27 T. Kang, F. Li, S. Baik, W. Shao, D. Ling and T. Hyeon, *Biomaterials*, 2017, **136**, 98-114.
28 P. Reimer, N. Jähnke, M. Fiebich, W. Schima, F. Deckers, C. Marx, N. Holzknecht and S. Saini, *Radiology*, 2000, **217**, 152-158.
29 Q. Miao and K. Pu, *Adv. Mater.,* 2018, **30**, e1801778.
30 Y. Jiang, P. Upputuri, C. Xie, Y. Lyu, L. Zhang, Q. Xiong, M. Pramanik and K. Pu, *Nano Lett.*, 2017, **17**, 4964-4969.
31 J. Li and K. Pu, *Chem. Soc. Rev.*, 2019, **48**, 38-71.
32 Y. Jiang, X. Zhao, J. Huang, J. Li, P. K. Upputuri, H. Sun, X. Han, M. Pramanik, Y. Miao, H. Duan, K. Pu and R. Zhang, *Nat. Commun.*, 2020, **11**, 1857.
33 J. Liu, J. Shi, W. Nie, S. Wang, G. Liu and K. Cai, *Adv. Healthc. Mater.*, 2021, **10**, e2001207.
34 I. Chen, S. Ariizumi, M. Nakano and M. Yamamoto, *J. Gastroenterol.*, 2014, **49**, 117-125.
35 H. Han, Y. Qiu, Y. Shi, W. Wen, X. He, L. Dong, Y. Tan, Y. Long, H. Tian and H. Wang, *Theranostics*, 2018, **8**, 3268-3274.
36 M. Capurro, I. Wanless, M. Sherman, G. Deboer, W. Shi, E. Miyoshi and J. Filmus, *Gastroenterology*, 2003, **125**, 89-97.
37 T. Zhou, X. Liang, P. Wang, Y. Hu, Y. Qi, Y. Jin, Y. Du, C. Fang and J. Tian, *ACS Nano*, 2020, **14**, 12679-12696.
38 W. Mu, D. Jiang, S. Mu, S. Liang, Y. Liu and N. Zhang, *ACS Appl. Mater. Interfaces*, 2019, **11**, 23591-23604.
39 H. Yang, H. S. Liu, W. Hou, J. X. Gao, Y. Duan, D. Wei, X. Q. Gong, H. J. Wang, X. L. Wu and J. Chang, *J. Mater. Chem. B*, 2020, **8**, 251-259.
40 S. Qiao, F. Xin, M. Wu, Y. Zheng, B. Zhao, C. Zhang, X. Liu, Z. Wei and J. Liu, *J. Mate. Chem. B*, 2021, **9**, 5083-5091.
41 K. Wang, Z. Zhang, H. Tsai, Y. Liu, J. Gao, M. Wang, L. Song, X. Cao, Z. Xu, H. Chen, A. Gong, D. Wang, F. Cheng, and H. Zhu, *Cell Death Differ.*, 2021, **28**, 1222-1236.
42 X. N. Yu, Y. Deng, G. C. Zhang, J. Liu, T. T. Liu, L. Dong, C. F. Zhu, X. Z. Shen, Y. H. Li and J. M. Zhu, *ACS Appl. Mater. Interfaces*, 2020, **12**, 17193-17206.
43 Q. Li, K. Chen, W. Huang, H. Ma, X. Zhao, J. Zhang, Y. Zhang, C. Fang and L. Nie, *Cancer Lett.*, 2021, **496**, 169-178.
44 H. Deng, W. Shang, G. Lu, P. Guo, T. Ai, C. Fang and J. Tian, *ACS Appl. Mater. Interfaces*, 2019, **11**, 14526-14537.
45 N. Liao, Y. Shi, Y. Wang, F. Liao, B. Zhao, Y. Zheng, Y. Zeng, X. Liu and J. Liu, *Stem Cell Res. Ther.*, 2020, **11**, 237.
46 G. Liu, J. Zhu, H. Guo, A. Sun, P. Chen, L. Xi, W. Huang, X. Song and X. Dong, *Angew. Chem. Int. Ed. Engl.*, 2019, **58**, 18641-18646.
47 C. Yin, X. Li, G. Wen, B. Yang, Y. Zhang, X. Chen, P. Zhao, S. Li, R. Li, L. Wang, C. Lee and L. Bian, *Biomaterials*, 2020, **232**, 119684.
48 J. Chen, Y. Zhang, X. Li, J. Zhu, D. Li, S. Li, C.-S. Lee and L. Wang, *Photonics Research*, 2020, **8**, 1875.
49 G. Wen, X. Li, Y. Zhang, X. Han, X. Xu, C. Liu, K. Chan, C. Lee, C. Yin, L. Bian and L. Wang, *ACS Appl. Mater. Interfaces*, 2020, **12**, 33492-33499.
50 Y. Zhang and L. Wang, *IEEE Trans. Med. Imaging*, 2020, **39**, 4369-4375.
51 L. Nicole, C. Laberty-Robert, L. Rozes and C. Sanchez, *Nanoscale*, 2014, **6**, 6267-6292.
52 W. Feng, X. Han, R. Wang, X. Gao, P. Hu, W. Yue, Y. Chen and J. Shi, *Adv. Mater.*, 2019, **31**, e1805919.
53 X. Zhen, K. Pu and X. Jiang, *Small*, 2021, **17**, e2004723.
54 S. Hu and L. V. Wang, *Biophys. J.*, 2013, **105**, 841-847.
55 R. Guo, Z. Wu, J. Wang, Q. Li, S. Shen, W. Wang, L. Zhou, W. Wang, Z. Cao and Y. Guo, *Adv. Sci.*, 2019, **6**, 1801885.
56 L. Li, L. Zhu, C. Ma, L. Lin, J. Yao, L. Wang, K. Maslov, R. Zhang, W. Chen, J. Shi and L. V. Wang, *Nat. Biomed. Eng.*, 2017, **1**, 0071.
57 S. Golombek, J. May, B. Theek, L. Appold, N. Drude, F. Kiessling and T. Lammers, *Adv. Drug Deliv. Rev.*, 2018, **130**, 17-38.
58 H. B. El-Serag, *N. Engl. J. Med,* 2011, **365**, 1118-1127.
59 K. Tzartzeva, J. Obi, N. Rich, N. Parikh, J. Marrero, A. Yopp, A. Waljee and A. Singal, *Gastroenterology*, 2018, **154**, 1706-1718.
60 K. J. Francis, R. Booijink, R. Bansal and W. Steenbergen, *Sensors*, 2020, **20**.
61 O. Rom, G. Xu, Y. Guo, Y. Zhu, H. Wang, J. Zhang, Y. Fan, W. Liang, H. Lu, Y. Liu, M. Aviram, Z. Liu, S. Kim, W. Liu, X. Wang, Y. E. Chen and L. Villacorta, *EBioMedicine*, 2019, **41**, 62-72.
62 Y. Koyama and D. Brenner, *J. Clin. Invest.*, 2017, **127**, 55-64.

63 P. van den Berg, R. Bansal, K. Daoudi, W. Steenbergen and J. Prakash, *Biomed. Opt. Express*, 2016, **7**, 5081-5091.

64 M. Karmacharya, L. Sultan, B. Kirkham, A. Brice, A. Wood and C. Sehgal, *Diagnostics (Basel)*, 2020, **10**, 705.

65 K. Shou, C. Qu, Y. Sun, H. Chen, S. Chen, L. Zhang, H. Xu, X. Hong, A. Yu and Z. Cheng, *Adv. Funct. Mater.*, 2017, **27**, 1700995.

66 C. Cheng, G. Tietjen, J. Saucier-Sawyer and W. Saltzman, *Nat. Rev. Drug Discov.*, 2015, **14**, 239-247.

67 C. Walkey, J. Olsen, H. Guo, A. Emili and W. Chan, *J. Am. Chem. Soc.*, 2012, **134**, 2139-2147.

68 M. Serper, T. Taddei, R. Mehta, K. D'Addeo, F. Dai, A. Aytaman, M. Baytarian, R. Fox, K. Hunt, D. Goldberg, A. Valderrama and D. Kaplan, *Gastroenterology*, 2017, **152**, 1954-1964

69 C. Peng, Y. Shih, P. Lee, T. Hsieh, T. Luo and M. Shieh, *ACS Nano*, 2011, **5**, 5594-5607.

70 G. Zhang, Y. Liao and I. Baker, *Mater. Sci. Eng. C. Mater. Biol. Appl.*, 2010, **30**, 92-97.

71 S. Sharifi, S. Behzadi, S. Laurent, M. Forrest, P. Stroeve and M. Mahmoudi, *Chem. Soc. Rev.*, 2012, **41**, 2323-2343.